International Journal of Nanoelectronics and Materials
IJNeaM
ISSN 1985-5761 | E-ISSN 2232-1535

Effect of rotational speed on structural and magnetic properties of cobalt ferrite substituted aluminium ions using coprecipitation method

Suharno[a*], Wisnu Pamungkas[b], Utari[b], Riyatun[b], Budi Purnama[b], and Nuryani[b]

[a]*Department of Physics Education, Faculty of Teacher Training and Education Universitas Sebelas Maret, 57126, Surakarta, Indonesia*
[b]*Department of Physics, Faculty of Mathematics and Natural Sciences Universitas Sebelas Maret, 57126, Surakarta, Indonesia*
∗ *Corresponding author. Tel.: +62-271-669124; fax: +62-271-648939; e-mail: suharno_71@staff.uns.ac.id*

Received 12 November 2024, Revised 9 August 202, Accepted 10 September 2025

ABSTRACT

The synthesis of Al-doped cobalt ferrite has been successfully carried out by the coprecipitation method. The synthesis method with varying rotational speeds aims to find the best characteristics for applications in military industrial technology, such as anti-radar detection materials. Variations in rotational speeds in the titration stage were followed by annealing at 1000°C for 3 hours. The results of this study found that all samples have a cubic structure, have two absorption peaks as octahedral and tetrahedral sides, and all samples are ferromagnetic, so they have the potential to be good anti-radar detection materials. Another finding is that samples without rotational speed are soft magnetic, which is most suitable for anti-radar detection applications.

Keywords: *Cobalt ferrite, Co-precipitation, Aluminium ion, Rotational speed, Cubic, Ferromagnetic*

1. INTRODUCTION

The development of magnetic materials has attracted the attention of many researchers, one of which is the ferrite magnetic material. One of the most studied ferrite magnetic materials is $CoFe_2O_4$ (Cobalt Ferrite). Cobalt Ferrite material has a high coercive (Hc) field [1,2], saturation magnetization (Ms), high magnetocrystalline anisotropy, as well as chemical stability and good mechanical strength [3], to potentially achieve superparamagnetic properties. Moreover, the physical characteristics of cobalt ferrite can be altered by substitution with metal ions and rare earth metal ions [4]. Cobalt ferrite belongs to a hard magnetic material having a high coercive field of up to 5400 Oe and a saturation magnetization of up to 80 emu/g [5].

The superiority of the magnetic properties of cobalt ferrite makes it applicable in technologies such as recording media, magnetic imaging resonance (MRI), microelectronic systems, chemistry [5], as well as drug delivery [6]. Several other case studies of the application of cobalt ferrite-based materials are cobalt ferrite as an antibacterial material [7], for photocatalytic applications [8-10], and as a microwave absorber [11,12].

Cobalt ferrite has been widely developed with several synthesis methods, such as coprecipitation methods [13,14], hydrothermal [15], and sol-gel autocombustion [16]. The sol gel autocombustion are a method of forming nanoparticles by a heating process at a certain temperature to form a sol-gel, which is then heated to dry at a certain temperature. The process of forming the solution phase into a sol-gel is not easy because it uses high temperatures.

The coprecipitation method is a method of forming nanoparticles by the process of precipitation of more than one substance together. This method can control the particle size, and the growth time is relatively short. Stages of reaction in this method include the process of nucleation, growth, hardening, and agglomeration. The nucleation and growth process greatly influences the particle size and morphology of the material [11]. The particle size is capable of changing the magnetic properties of multiple domains into a single domain. In addition, annealing temperatures are able to modify particle size [18-21].

This research was conducted on the synthesis of cobalt ferrite doped with aluminum using the coprecipitation method. Variations in rotational speed were carried out to obtain the effect of rotational speed on changes in crystal structure, shifts in absorption peaks, and other physical properties, so that they can modify the magnetic properties of cobalt ferrite-based materials and add new knowledge through theoretical physics studies.

Cobalt ferrite synthesis has been carried out through variations in heating and doping types, but no research has been found on the effect of rotational speed on the synthesis process, on changes in crystal structure, changes in magnetic properties, and other physical properties. Therefore, the significance of this study is that differences in rotational speed through the coprecipitation synthesis method can affect the physical properties of materials applied as photocatalysts to reduce air pollution and as anti-radar detection materials for military technology or other industrial technologies.

2. MATERIAL AND METHOD

$Al(NO_3)_2.9H_2O$ of 0.001 mol, 0,01 mol $Co(NO_3)_2.6H_2O$ and 0.019 mol $Fe(NO_3)_3.9H_2O$ dissolved in 200 ml aquabides. Then the solution was stirred by using a magnetic stirrer placed on a Hotplate that has a rotational speed of 250 rpm. The titration process was carried out using a solution of NaOH 4.8 M as much as 100 ml at 85°C synthesis temperature. This situation took place in a stirring process using a magnetic stirrer above a hotplate with constant synthesis temperature at 85°C. Then, the result of the titration is called the co-precipitant. Furthermore, the process of precipitating precipitation with the ultraspeed centrifuge is varied at rotational speed (0 rpm or without centrifuge, 1000 rpm, 2000 rpm, 4000 rpm). The washing process was carried out using ethanol and aquabides. Hydrolysis process with temperature 100°C for 12 hours, as the process of drying and collecting process of the samples was done for 1 hour. Furthermore, the annealing process was performed at a temperature of 1000°C for 5 hours. and collected for 2 hours and obtained samples were **S1** = $CoAl_{0.1}Fe_{1.9}O_4$ 0 rpm, **S2** = $CoAl_{0.1}Fe_{1.9}O_4$ 1000 rpm, **S3** = $CoAl_{0.1}Fe_{1.9}O_4$ 2000 rpm, and **S4** = $CoAl_{0.1}Fe_{1.9}O_4$ 4000 rpm.

The samples were then analyzed using a Bruker D8 Advance X-ray diffractometer (XRD) with Cu-Kα radiation (λ = 1.54 Å) to analyze their crystal structure in the 2θ range of 20°-80° to determine crystal structure, crystallite size, density, and lattice strain. The chemical bonds of the samples were identified with Shimadzu IF Prestige 21 Fourier Transform Infrared (FTIR) spectroscopy in the wavenumber range of 350 cm^{-1} – 4000 cm^{-1}. Meanwhile, the magnetic properties were analyzed via Quantum Design PPMS VersaLab Vibrating Sample Magnetometer (VSM) at room temperature.

3. RESULT AND DISCUSSION

3.1. Structural

The XRD characteristic results of a cobalt ferrite doped aluminum ion sample of coprecipitation synthesis results with additional treatment or centrifuge treatment for variations of 0 rpm or no centrifuge rotation speed, 1000 rpm, 2000 rpm, and 4000 rpm samples of cobalt ferrite doping of aluminum ion are synthesized at 85°C and annealing temperature 1000°C for 3 hours, are shown in Figure 1. The pattern of XRD characterization results shows the suitability of the peaks that arise with the number of ICDD data 221086. This shows that the sample has an inverse spinel face-centered cubic (fcc) structure.

When samples were without a centrifuge or 0 rpm, the highest intensity of XRD results was observed at an angle of 35.43°. Or, in other words, just shifted 0.01° from ICDD 221086 data. With the addition of centrifuge treatment, the speed of rotation causes the 2θ angle to shift to the right. For a rotational speed of 1000 rpm, the angle (2θ) is observed to be 35.49° (or shifted by 35.49°- 35.44° = 0.05°). For rotational speed 2000 rpm and 4000 rpm, each shifted by 0.07° and 0.11°. This indicates a change in crystallite size without changing the main structure of the inverse spinel fcc. It is seen that the rotational velocity affects the crystal alteration size, with the change of the crystallite size not showing regularity.

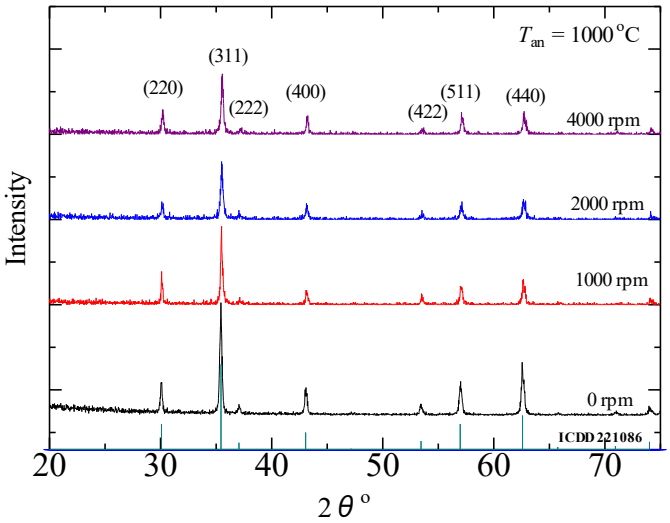

Figure 1. The diffraction patterns of the $CoAl_{0.1}Fe_{1.9}O_4$ sample with rotational speed variation

Table 1. Crystallite size (D), density (d), and lattice strains (ε)

Samples	D (nm)	d (gr/cm³)	ε (·10³)
S1	38.77	5.33	2.93
S2	34.98	5.36	3.35
S3	28.57	5.37	3.97
S4	31.81	5.38	3.56

In Table 1, it appears that the four samples show different crystallite sizes. At a rotation speed of 0 rpm or without a centrifuge crystallite size is 38.77 nm. However, with increased rotational speed (1000 rpm, 2000 rpm, and 4000 rpm), the crystallite size of each was 34.98 nm, 28.57 nm, and 31.81 nm. Determination of crystallite size using the Scherrer equation with the equation:

$$D = \frac{k\lambda}{\beta \cos\theta} \quad (1)$$

where D is the crystallite size, k is the Scherrer constant (0.89), λ is the wavelength of X-ray Cu-Kα = 0.15 nm, β is the full width of the diffraction line at half maximum intensity (FWHM) in radians, and θ is the Bragg angle.

Observed from the curve in Figure 2(a), that the addition of the centrifuge treatment resulted in a significantly decreased crystallite size. It is possible that the increasing centrifugation causes the lattice parameters to decrease, so that the spacings between the crystallite planes are closer together, resulting in decreased crystallite size. The phenomenon in Figure 2(a) is related to Figure 2(c), which is likely caused by the material experiencing a decrease in strain, which can cause distortion in the crystal structure, and the material undergoes recrystallization to form larger crystallites. Another cause is that in polycrystalline materials, crystal growth can generally occur through grain

boundary movement, and these grains can merge with the surrounding grains

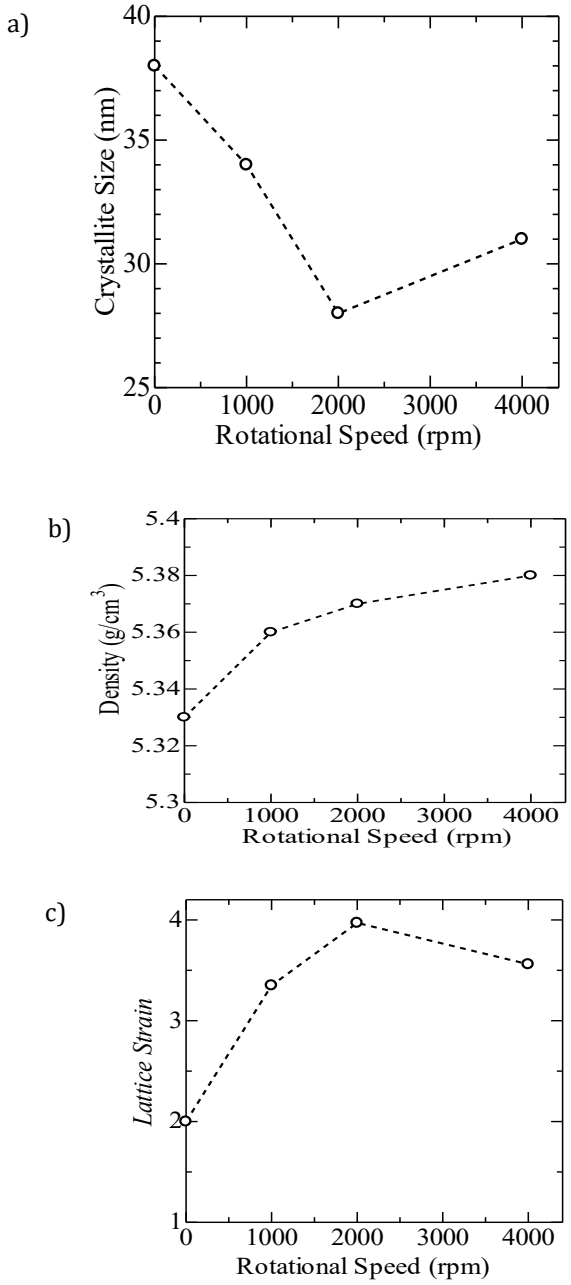

Figure 2. The Effect of rotation speed curve (rpm) on (a) crystallite size, (b) density, and (c) lattice strain

increasing the average crystallite size. Figure 2(b), It is clearly observed that the density increases with increasing rotational speed. The density value increased from 5.33 g/cm^3 to 5.38 g/cm^3 as the rotational speed increased from 0 rpm to 4000 rpm. It is alleged that the increase in centrifugation suppresses the lattice parameter decrease so that the density value between the crystallites increases. Figure 2(c) shows that the increase in rotational velocity affects the lattice strain value in Table 1. At a rotation speed of 0 rpm or without a centrifuge of $2.93 \cdot 10^{-3}$. However, with an increase in rotational speed (1000 rpm, 2000 rpm, and 4000 rpm), lattice strains were respectively $3.35 \cdot 10^{-3}$, $3.97 \cdot 10^{-3}$, and $3.56 \cdot 10^{-3}$. The x-ray of density (ρ_x) and lattice strain (ε) can be calculated by the following equations :

$$\rho_x = \frac{8M}{2a^3} \quad (2)$$

$$\varepsilon = \frac{\beta}{4\tan\theta} \quad (3)$$

where M is the molecular weight of the sample, a^3 is the cell volume of the sample. Observed from the curve that the addition of a centrifuge treatment resulted in an increase in the value of the lattice strain. It is possible that a decrease in the crystallite size value results in an increase in the lattice strain value. Decreased crystallite size and increased lattice strain in the presence of aluminum doping are consistent with the results reported [4]. The decrease in lattice strain can occur due to recrystallization involving the formation of new strain-free grains, where, when the grains grow, they can eliminate the distortion that has an impact on the decrease in lattice strain. Thus, the decrease in lattice strain is related to the increase in crystal size, as shown in Figure 2(a).

Table 2 shows that the increase in rotational velocity affects lattice parameter values, with the lattice parameter value decreasing from 8.39 Å to 8.36 Å. In theory, the decrease of lattice parameter a has an effect on the density value.

Table 2. The rietveld analysis parameters of **S1, S2, S3,** and **S4**

Parameters	The samples			
	S1	**S2**	**S3**	**S4**
R_p	53.80	54.80	56.40	54.00
R_{wp}	56.20	43.40	43.88	42.00
R_B	10.46	13.00	10.50	9.81
χ^2	1.63	1.16	1.19	1.14
a,b,c (Å)	8.39	8.38	8.37	8.36

Crystal structure analysis was carried out using the Rietveld method using Fullprof to determine the difference in the intensity of the diffraction pattern of the experimental results with calculations through the calculation of the R factor parameters obtained. The R factor is calculated using the equation :

$$R_{wp} = 100\left[\frac{\sum_{i=1}^{n} w_i|y_i - y_{c,i}|^2}{\sum_{i=1}^{n} w_i y_i{}^2}\right]^{\frac{1}{2}} \quad (4)$$

$$R_{exp} = 100\left[\frac{n-p}{\sum_{i=1}^{n} w_i y_i{}^2}\right]^{\frac{1}{2}} \quad (5)$$

$$R_B = 100\frac{\sum_{i=1}^{n}|I_{obs} - I_{cal}|}{\sum_{i=1}^{n} I_{obs}} \quad (6)$$

$$\chi^2 = \left[\frac{R_{wp}}{R_{exp}}\right]^2 \quad (7)$$

The Rietveld analysis parameters at the crystal system cubic and space group Fd-3m of the samples. The analysis of the crystal structure of the synthesized cobalt ferrite in this study was carried out using Rietveld analysis [22-23]. The Bragg diffraction or thick mark in the Fd-3m group

space is indicated by a vertical line below the peak of the diffraction pattern, identified as the cobalt ferrite phase. The diffraction pattern from the Rietveld analysis shows a very small difference between the calculation and the experimental results. This shows that the results of the Rietveld analysis are very good. The Rietveld analysis process is corrected against the background of the pseudo-Voigt function.

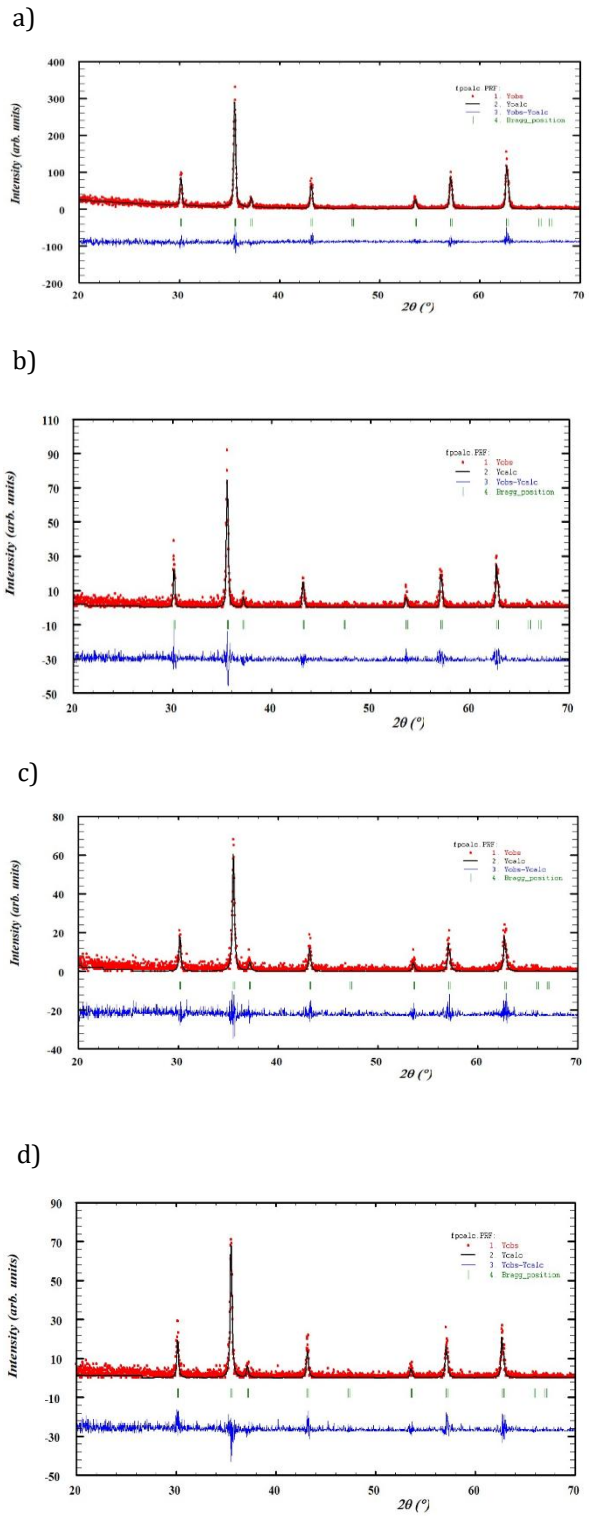

Figure 3. The diffraction pattern graphs from rietveld analysis of samples (a) **S1**, (b) **S2**, (c) **S3**, and (d) **S4**

3.2. Fourier Transform Infra-Red (FTIR) Spectra

Figure 4 shows the result of FTIR spectra synthesized at 85°C synthesis temperature and 1000°C annealing temperature with rotation speed variation 0 rpm or without centrifuge, 1000 rpm, 2000 rpm, and 4000 rpm. It can be seen in the figure that the characteristics of this absorption curve are found in wave numbers around 400-600 $cm^{-1,}$ which are common characteristics of spinel ferrite. The highest-frequency uptake band is located around 600 cm^{-1} which is regarded as a vibrating stretch of a tetrahedral metal complex consisting of bonds between oxygen ions and metal ions at the tetrahedral site and whereas the lower absorption bands located around 400 cm^{-1} wave number are regarded as bending vibrations of octahedral metal complexes consisting of bonds between oxygen ions and metal ions at the octahedral site [24]. This result is in accordance with a study conducted on the cobalt ferrite spinel oxide compound [25].

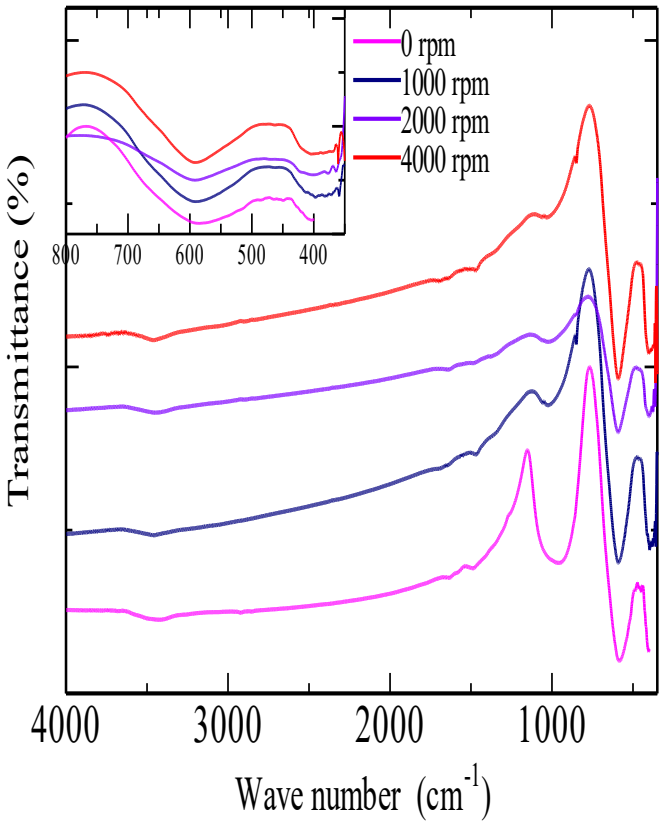

Figure 4. FTIR Spectra of $CoAl_{0.1}Fe_{1.9}O_4$ with rotational speed variation

Table 3 shows the results of the calculation of force constants in the tetrahedral site and the octahedral site of the aluminum ion ferrite doping cobalt. Also, the results of the fourth wave number of the sample show that the presence of centrifuge treatment has an effect on the shift of wave numbers in the tetrahedral site and octahedral site. The characterization results show the same trend between k_1 and k_t to increase the rotational speed/ centrifuge of the ferrite cobalt sample with aluminum doping.

Table 3. Absorption peak (k_1 dan k_2), force constant in tetrahedral (k_t), and octahedral (k_0) of $CoAl_{0.1}Fe_{1.9}O_4$

Samples	k_1(cm^{-1})	k_2 (cm^{-1})	k_t (N/m)	k_0 (N/m)
S1	584.46	449.43	14.54	12.31
S2	591.21	397.35	14.87	9.62
S3	592.17	400.25	14.92	9.76
S4	591.21	404.10	14.87	9.95

From the table, it can be seen that at the octahedral site, the sample with a rotational speed of 0 rpm or without a centrifuge has a style constant of 12.31 N/m. However, when centrifuge treatment with rotational speed (1000 rpm, 2000 rpm, and 4000 rpm) was performed, the force constant at the octahedral site decreased (9.62 N/m, 9.76 N/m, and 9.95 N/m, respectively). While on the tetrahedral site, there is an irregularity of constant style values where the increase or decrease is not so significant, that is, in the sample with rotation speed 0 rpm or without centrifuge, which is equal to 14.54 N/m. However, when the centrifuge treatment was added (1000 rpm, 2000 rpm, 4000 rpm), the result of the force constant at the tetrahedral site was 14.87 N/m, 14.92 N/m, 14.87 N/m.

These results indicate that the increased rotational speed is more pressing on the octahedral site due to significant shifting force constants, so that the change in rotational velocity is more influential on the change of octahedral site constant than the tetrahedral site constants. So it can be said that the lattice strain occurs inside the octahedral, where the addition of the centrifuge treatment causes a shift in the lattice strain value. From XRD and FTIR data, can be determined the elasticity properties of samples, such as Bulk Modulus, Rigidity Modulus, and Young's Modulus, can be determined, as shown in Figure 5. Figure 5 shows the same pattern, where the three moduli decrease at a rotational speed of 0 rpm or without centrifuge to 1000 rpm. Then experience an increase in rotation speed from 1000 rpm to 4000 rpm. This indicates that an increase in rotational velocity affects changes in Bulk Modulus (B), Rigidity Modulus (G), and Young's Modulus (E).

Table 4. The rotational speed against Bulk Modulus (B), Young's Modulus (E), and Rigidity Modulus (G)

Samples	B ($dyne/cm^2$)	E ($dyne/cm^2$)	G ($dyne/cm^2$)
S1	$0.79 \cdot 10^{11}$	$1.45 \cdot 10^{11}$	$0.61 \cdot 10^{11}$
S2	$0.72 \cdot 10^{11}$	$1.33 \cdot 10^{11}$	$0.56 \cdot 10^{11}$
S3	$0.73 \cdot 10^{11}$	$1.34 \cdot 10^{11}$	$0.56 \cdot 10^{11}$
S4	$0.73 \cdot 10^{11}$	$1.35 \cdot 10^{11}$	$0.57 \cdot 10^{11}$

The behavior of these three moduli is related to the strengthening of bonds between atoms and spinel lattice atoms. Table 4 shows that Young's Modulus (E), or the tendency of an object to deform along the axis, decreased by centrifuge treatment. From the table, there is also a change in the Rigidity Modulus (G) or the tendency of an object to deform on a fixed volume. Where the centrifuge treatment resulted in Rigidity Modulus (G) decreased due to centrifuge treatment. The table also shows the value of Bulk Modulus (B) due to the centrifuge treatment. Bulk Modulus (B) is the tendency of an object to deform in all directions when given a uniform stress in all directions. Bulk Modulus (B) has decreased when given a centrifuge treatment [26]. These results indicate that the decrease in the value of all three moduli is possible due to an increase in the density of the sample. The fact that density has a great effect on the elastic modulus may be due to the fact that the ferrite sample has a different density.

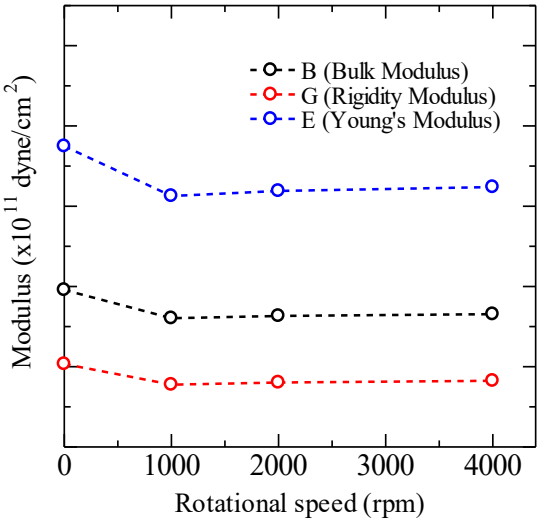

Figure 5. The rotational speed effect curves on Bulk Modulus (B), Rigidity Modulus (G), and Young's Modulus (E)

3.3. Magnetic properties

Figure 6 shows the results of hysterical curve of the cobalt ferrite doped aluminum ion sample with variation of rotational speed, then annealing at a temperature 1000°C. From the figure, it is seen that the four samples show different forms of a hysteresis curve. When not with a centrifuge treatment or a 0 rpm rotational speed, the hysteresis curve is high, but the coercivity is small. However, with an increase in rotational speed (1000 rpm, 2000 rpm, and 4000 rpm), the curve decreases with coercivity that tends to increase..

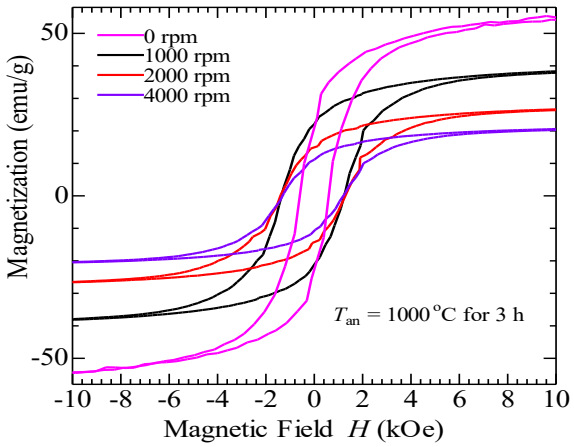

Figure 6. The hysteresis curve of $CoAl_{0.1}Fe_{1.9}O_4$ with rotational speed variation

Table 5. The parameter magnetic of $CoAl_{0.1}Fe_{1.9}O_4$ with rotational speed variation

Samples	Mr (emu/g)	Ms (emu/g)	Hc (kOe)	Mr/Ms (kOe)
S1	24.88	56.39	0.53	0.44
S2	31.32	38.36	1.28	0.56
S3	14.53	26.62	1.29	0.54
S4	10.77	20.64	1.26	0.52

Observed from the curve that the greater the rotational speed, there is a significant decrease in magnetization. This indicates that magnetization is influenced by rotational speed. Table 5 shows the magnetic characteristic changes disclosed with Mr, Ms, Hc, and Mr/Ms due to rotational speed, and it can be seen that the change in rotational velocity indicates a change of remanent magnetization (Mr), saturation magnetization (Ms), coercive field (Hc), and squarness ratio (Mr/Ms). The squarness ratio shows the baldness of the hysteresis curve, so that the greater the squarness ratio, the more proportional to the coercive field the resulting hysteresis curve, the better the magnetic property, where the squarness ratio is approximately one [27-29]. So it is pointed out that the increase in rotation speed affects the magnetic properties of the sample. In Figure 7(a), the saturation magnetization changes due to an increase in rotational speed. It is possible that the crystal structure is an inverse spinel fcc, where there is an octahedral site and a tetrahedral site. Thus, the redistribution of cations at the octahedral site and the tetrahedral site results in a decrease in saturation magnetization [30-32]. Figure 7(b) shows the change in Hc due to the influence of rotational speed. This indicates that the precipitation process results in the magnetic depinning domain at the interface. While the increase in rotational speed does not significantly increase the magnetic depinning domain that occurs, the coercive field obtained does not significantly change.

a)

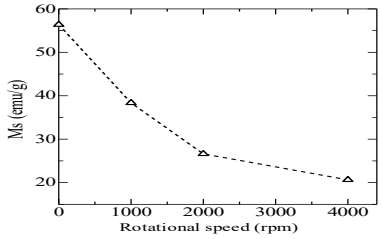

b)

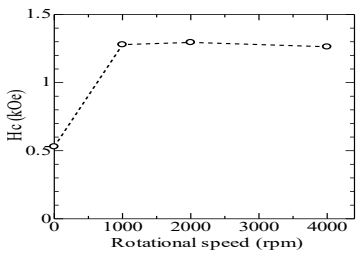

Figure 7. The rotational speed effect curve to (a) saturation magnetization (Ms) and (b) coercivity (Hc)

The effect of different rotational speeds on the cobalt ferrite synthesis process affects the smaller particle size, and particle size is related to crystallite size. The results of this study show that smaller crystal sizes have an impact on increasing magnetic coercivity. This phenomenon is caused by several physical properties of cobalt ferrite materials such as smaller crystallites can cause an increase in domain walls, which can increase coercivity, smaller crystallites have a larger surface to volume ratio which can cause an increase in surface anisotropy and defects and these defects can pinch domain walls thereby increasing coercivity, in smaller crystallites the exchange interaction between adjacent grains causes changes in magnetic properties, including coercivity.

The application of cobalt ferrite-based materials for economic and energy benefits is as battery electrode materials [33]. While the environmental impact benefits are cobalt ferrite-based materials as photocatalyst materials for efforts to reduce air pollution [8,9], as a sustainable technology to reduce environmental impacts. Research on cobalt ferrite materials as photocatalyst materials continues to be carried out sustainably to obtain the best materials as photocatalyst materials.

Therefore, to realize this research to obtain optimal results, collaboration is needed with institutions or research across related scientific fields, such as advanced material research in the field of materials engineering and environmental science, or communication technology related to the application of cobalt ferrite materials.

4. CONCLUSION

Based on the results and discussion, the results of this study indicate that the modification of the rotational speed of Al-doped cobalt ferrite has a significant effect on the physical characteristics. The results of the crystal structure analysis show that Al-doped cobalt ferrite has a cubic structure, and variations in rotational speed affect the crystallite size, density, and lattice strain. The FTIR test results show two absorption peaks for the octahedral and tetrahedral sides. Magnetic properties indicate that increasing the rotational speed has an impact on increasing the coercivity field, and all samples are ferromagnetic. The characteristics of the data from this study can be used as a basis for analysis to be applied in engineering Al-doped cobalt ferrite materials in anti-radar detection technology. Specifically, it was found that Al-doped cobalt ferrite without rotational speed is the best soft magnetic material, so it is best used as a microwave absorber material or anti-detection material, and other findings with a rotational speed of 200 rpm have the smallest crystal size, which has the potential to be the best photocatalyst material. Therefore, the direction of further research is the synthesis of Al-doped cobalt ferrite without rotational speed can be selected as anti-radar detection, and synthesis through rotational speed of 200 rpm can be selected as a photocatalyst material to find the best properties through annealing variations.

ACKNOWLEDGMENTS

This research was funded by the Agreement letter research implementation assignment, DIPA Non APBN Universitas Sebelas Maret, number 194.2/UN27.22/PT.01.03/2024.

REFERENCES

[1] P. Motavallian, B. Abasht, O. Mirzaee, and H. Abdollah-Pour, "Correlation between structural and magnetic properties of substituted (Cd, Zr) cobalt ferrite nanoparticles," *Chinese Journal of Physics*, vol. 57, pp. 6–13, 2019.

[2] J. Das, V. S. Moholkar, and S. Chakma, "Structural, magnetic and optical properties of sonochemically synthesized Zr-ferrite nanoparticles," *Powder Technology*, vol. 328, pp. 1–6, 2018.

[3] S. Chakrabarty, A. Dutta, and M. Pal, "Effect of yttrium doping on structure, magnetic and electrical properties of nanocrystalline cobalt ferrite," *Journal of Magnetism and Magnetic Materials*, vol. 461, pp. 69–75, 2018.

[4] K. V. Kumar, D. Paramesh, and P. V. Reddy, "Effect of Aluminium Doping on Structural and Magnetic Properties of Ni-Zn Ferrite Nanoparticles," *World Journal of Nano Science and Engineering*, vol. 5, no. 3, pp. 68–77, 2015.

[5] N. Hosni, K. Zehani, T. Bartoli, L. Bessais, and H. Maghraoui-Meherzi, "Semi-hard magnetic properties of nanoparticles of cobalt ferrite synthesized by the co-precipitation process," *Journal of Alloys and Compounds*, vol. 694, pp. 1295–1301, 2017.

[6] S. Hatamie, Z. M. Balasi, M. M. Ahadian, T. Mortezazadeh, F. Shams, and S. Hosseinzadeh, "Hyperthermia of breast cancer tumor using graphene oxide-cobalt ferrite magnetic nanoparticles in mice," *Journal of Drug Delivery Science and Technology*, vol. 65, p. 102680, 2021.

[7] D. Gheidari, M. Mehrdad, S. Maleki, and S. Hosseini, "Synthesis and potent antimicrobial activity of $CoFe_2O_4$ nanoparticles under visible light," *Heliyon*, vol. 6, no. 10, p. e05058, Oct. 2020.

[8] M. K. Shobana, G. Nandhini, S. Kavita, V. Suresh Kumar, and T. Pazhanivel, "Photocatalytic and magnetic properties of Mg substituted cobalt ferrite," *Materials Science and Engineering: B*, vol. 286, p. 116030, Dec. 2022.

[9] Y. Guo, C. Ren, L. Li, and X. Zhang, "Comparative Study of Cobalt Ferrite and Polyacrylamide Decorated Cobalt Ferrite Microspheres in Structural, Optical, Magnetic, Photoluminescence, and Photocatalytic Properties," *Russian Journal of Physical Chemistry A*, vol. 94, no. 12, pp. 2614–2621, Dec. 2020.

[10] H. Kumar, A. Giri, and A. Rai, "Photocatalytic degradation of naphthol blue black dye using undoped and Al-doped cobalt ferrite nanoparticles," *Kuwait Journal of Science*, vol. 51, no. 2, p. 100208, Apr. 2024.

[11] M. Kaur and S. Bahel, "Microwave absorption characteristics of cobalt doped zinc spinel ferrites in Ku-band (12.4–18 GHz)," Materials Today: Proceedings, vol. 82, pp. 1–7, 2023.

[12] N. Aggarwal and S. B. Narang, "Comparison of microwave absorption characteristics of Co-Zr substituted Ni-Zn ferrites and Mg-Zr substituted Ni-Zn ferrites in Ka band (26.5 – 40 GHz)," Materials Today: Proceedings, vol. 50, pp. 1892–1899, 2022.

[13] Ibrahim, S. M., Badawy, A. A., & Essawy, H. A., "Improvement of dyes removal from aqueous solution by Nanosized cobalt ferrite treated with humic acid during coprecipitation," Journal of Nanostructure in Chemistry, vol. 9, issue 4, pp. 281–298, 2019.

[14] S. Moosavi, S. Zakaria, C. H. Chia, and S. Gan, "Synthesize and characterization of nanostructure magnetic cobalt ferrite using hydrothermal method," AIP Conference Proceedings, 2016.

[15] S. M. Hashemi, Z. Ataollahi, S. Hasani, and A. Seifoddini, "Synthesis of the cobalt ferrite magnetic nanoparticles by sol–gel auto-combustion method in the presence of egg white (albumin)," Journal of Sol-Gel Science and Technology, vol. 106, issue 1, pp. 23–36, 2023.

[16] Kotnala, R.K., & Shah, Jyoti., "Ferrite Materials," Handbook of Magnetic Materials, pp. 291–379, 2015.

[17] C. Chitra, T. Raguram, and K. S. Rajni, "Microstructural and Magnetic Properties of Cobalt Ferrite Nanoparticles Synthesized by Sol-Gel Technique," International Journal of Trend in Scientific Research and Development, vol. 2, Issue 5, pp. 371–377, 2018.

[18] Daffe, N., Choueikani, F., Neveu, S., Arrio, M.-A., Juhin, A., Ohresser, P., Dupuis, V., & Sainctavit, P., "Magnetic anisotropies and cationic distribution in CoFe2O4 nanoparticles prepared by co-precipitation route: Influence of particle size and stoichiometry," Journal of Magnetism and Magnetic Materials, vol. 460, pp. 243–252, 2018.

[19] G. R. Patta, V. C. Babu, V. R. Kumar, and N. Veeraiah, "Study on the influence of gelation promoter on the structural and magnetic properties of cobalt ferrite nanoparticles developed through sol-gel method," Journal of Sol-Gel Science and Technology, vol. 100, no. 2, pp. 310–325, 2021.

[20] N. Hamdi, L. Bessais, and W. Belam, "Sol-gel Autocombustion Elaboration and Physiochemical Characterizations of Cu2+ Substituted Cobalt Ferrite Nanoparticles," Open Chemistry Journal, vol. 7, no. 1, pp. 44–54. 2020.

[21] H. Bedi, S. Rohilla, and N. Chaudhary, "Investigation of annealing temperature on the synthesis of zincite doped cobalt ferrite using Rietveld refinement," Journal of Physics:

Conference Series, vol. 2070, no. 1, p. 012091, 2021.

[22] F. I. Hussain and A. J. Abbas, "Structural analysis for Nil-xZnxFe2O4 spinel ferrite by PXRD and rietveld refinement method," AIP Conference Proceedings, 2022.

[23] R. Safi, A. Ghasemi, R. Shoja-Razavi, and M. Tavousi, "The role of pH on the particle size and magnetic consequence of cobalt ferrite," *Journal of Magnetism and Magnetic Materials*, vol. 396, pp. 288–294, 2015.

[24] S. Hossain and S. Hossain, "Optical characterization of cobalt ferrite and magnetoelectric cobalt ferrite–barium titanate core shell nanoparticles in infra-red range," *IEEE Transactions on Nanotechnology*, vol. 21, pp. 172–176, 2022.

[25] M. Lipińska-Chwałek, F. Schulze-Küppers, and J. Malzbender, "Strength and elastic modulus of lanthanum strontium cobalt ferrite membrane materials," *Ceramics International*, vol. 41, no. 1, pp. 1355–1360, 2015.

[26] D. Parajuli, N. Murali, and K. Samatha, "Structural, morphological, and magnetic properties of nickel substituted cobalt zinc nanoferrites at different sintering temperature," *Journal of Nepal Physical Society*, vol. 7, no. 2, pp. 24–32, 2021.

[27] K. Rana, P. Thakur, P. Sharma, M. Tomar, V. Gupta, and A. Thakur, "Improved structural and magnetic properties of cobalt nanoferrites: Influence of sintering temperature," *Ceramics International*, vol. 41, no. 3, pp. 4492–4497, 2015.

[28] B. Purnama, R. Rafika, T. W. Agung, and Suharyana, "Dependence of structural and magnetic properties on annealing times in co-precipitated cobalt ferrite nanoparticles," *Journal of Magnetics*, vol. 20, no. 3, pp. 207–210, 2015.

[29] M. S. A. Darwish, "Magnetite zinc cobalt ferrite nanoparticles: Synthesis, magnetic behavior, and optical properties," *Crystals*, vol. 13, no. 8, p. 1284, 2023.

[30] J. Balavijayalakshmi and C. Annie Josphine, "Impact of annealing on structural and magnetic properties of manganese co-doped magnesium–cobalt ferrite nanoparticles," *Recent Trends in Materials Science and Applications*, pp. 233–243, 2017.

[31] R. Priyadharsini, P. Dhamodharan, M. Venkateshwarlu, and C. Manoharan, "Influence of cobalt on magnetic, dielectric and electrochemical properties of copper ferrite nanoparticles via hydrothermal method," *Solid State Sciences*, vol. 137, p. 107123, 2023.

[32] R. Arilasita, Suharno, B. Utari, and B. Purnama, "The control of structural and magnetic properties in bismuth substituted cobalt ferrite by heat treatment," *International Journal of Nanoelectronics and Materials*, vol. 14, no. 4, pp. 389–398, 2021.

[33] A. Olivo, B. Beyribey, H. Kim, and J. Persky, "Cobalt oxide enhanced lanthanum strontium cobalt ferrite electrode for solid oxide fuel cells," Main Group Chemistry, vol. 21, no. 1, pp. 195–207, 2022.